





Data Descriptor

High-Resolution Surface Water Classifications of the Xingu River, Brazil, Pre and Post Operationalization of the Belo Monte Hydropower Complex

Margaret Kalacska ^{1,*} , Oliver Lucanus ¹ , Leandro Sousa ²  and J. Pablo Arroyo-Mora ³ 

¹ Applied Remote Sensing Lab, Department of Geography, McGill University, Montreal, QC H3A 0B9, Canada; oliver.lucanus2@mcgill.ca

² Laboratório de Ictiologia de Altamira, Universidade Federal do Pará, Altamira, PA 68372-040, Brazil; leandro.m.sousa@gmail.com

³ Flight Research Lab, National Research Council, Ottawa, ON K1A-0R6, Canada; JuanPablo.Arroyo-Mora@nrc-cnrc.gc.ca

* Correspondence: margaret.kalacska@mcgill.ca

Received: 27 June 2020; Accepted: 26 August 2020; Published: 29 August 2020



Abstract: We describe a new high spatial resolution surface water classification dataset generated for the Xingu river, Brazil, from its confluence with the Iriri river to the Pimental dam prior to construction of the Belo Monte hydropower complex, and after its operationalization. This river is well-known for its exceptionally high diversity and endemism in ichthyofauna. Pre-existing datasets generated from moderate resolution satellite imagery (e.g., 30 m) do not adequately capture the extent of the river. Accurate measurements of water extent are important for a range of applications utilizing surface water data, including greenhouse gas emission estimation, land cover change mapping, and habitat loss/change estimates, among others. We generated the new classifications from RapidEye imagery (5 m pixel size) for 2011 and PlanteScope imagery (3 m pixel size) for 2019 using a Geographic Object Based Image Analysis (GEOBIA) approach.

Dataset: DOI number: <https://doi.org/10.6084/m9.figshare.12521900.v1>

Dataset License: CC-BY 4.0.

Keywords: Altamira; endemic; freshwater fish; land cover change; PlanetScope; RapidEye; reservoir; Worldview 1; *Hypancistrus zebra*; dam

1. Summary

The Xingu River, the fourth largest tributary of the Amazon basin, has exceptionally high ichthyological diversity, with more than 600 species of fish, including many endangered fishes, such as the zebra pleco (*Hypancistrus zebra*) [1–3]. It has been in the international spotlight over a high-profile land conflict since the mid-1970s: the construction of the hydroelectric complex of Belo Monte [4,5]. Dam construction in the Amazon is relative recent, beginning in earnest in the 1980s (e.g., Balbina, Tucuruí). The many dams built over the last few decades have been shown to lead to substantial losses of natural habitats and negative environmental effects on one of the most diverse biomes on the planet [6,7].

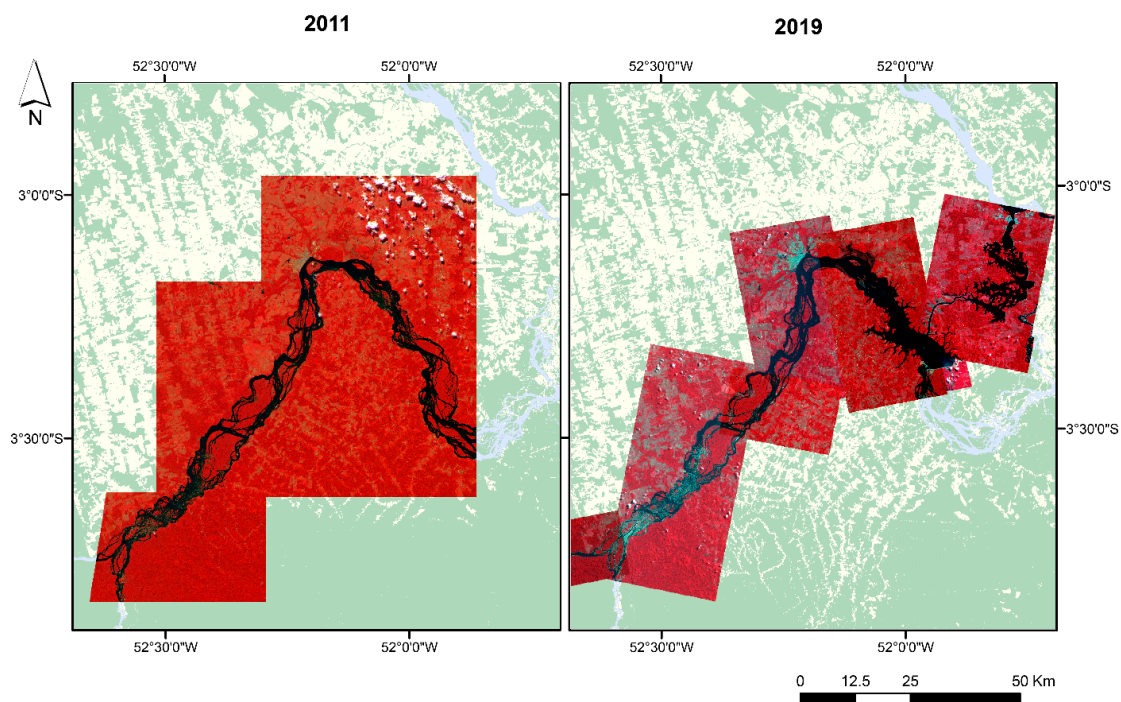
Efforts to study the impacts of the large scale landscape changes brought about by river impoundment and dam construction have been carried out for the Xingu and other rivers in the Amazon (for example [8–11]), but they rely primarily on pre-construction environmental impact assessments, data sources that may be out of date, or do not have the necessary spatial resolution to accurately document the changes (e.g., [12,13]). Continental-scale high-spatial resolution fluvial

mapping initiatives such as [14] are not yet available for South America. The data readily available to Brazilian agencies and others studying these regions are usually generated from moderate resolution images with pixel sizes of 30 m or more, and can lead to substantial uncertainties in calculations of impact area, greenhouse gas emissions, habitat loss, etc. [15]. In order to quantify the extent of the flooded area due to the main and artificial reservoirs of the dam, we developed a high spatial resolution surface water classification for 2011 (pre Belo Monte) and 2019 (after operationalization of the dam). These datasets were produced from RapidEye (5 m) and PlanetScope (3 m) imagery classified with a Geographic Object Based Image Analysis (GEOBIA) approach [14,16].

2. Data Description

The dataset for download from figshare (<https://doi.org/10.6084/m9.figshare.12521900.v1>) comprises two high-spatial resolution surface water maps (dry season) for 2011 and 2019. The extent of the surface water classification spans from the confluence of the Xingu and Iriri rivers to the Pimental dam, downstream of the city Altamira (Figure 1). For the 2019 dataset, the artificial reservoir is also included, beyond the power station where the outflow rejoins the Xingu river (Belo Monte dam). The datasets are provided as ESRI shapefiles and in Geotiff format (native 5 and 3 m pixel sizes, respectively). In the Geotiffs, pixels represent one of two classes: water (1) or land (0). All datasets are projected in UTM 22S WGS84.

A



Forest/ Non-Forest background layer source: Kalacska, M.; Lucanus, O.; Sousa, L.; Arroyo-Mora, J.P. A New Multi-Temporal Forest Cover Classification for the Xingu River Basin, Brazil. Data 2019, 4: 114.

Figure 1. Cont.

B

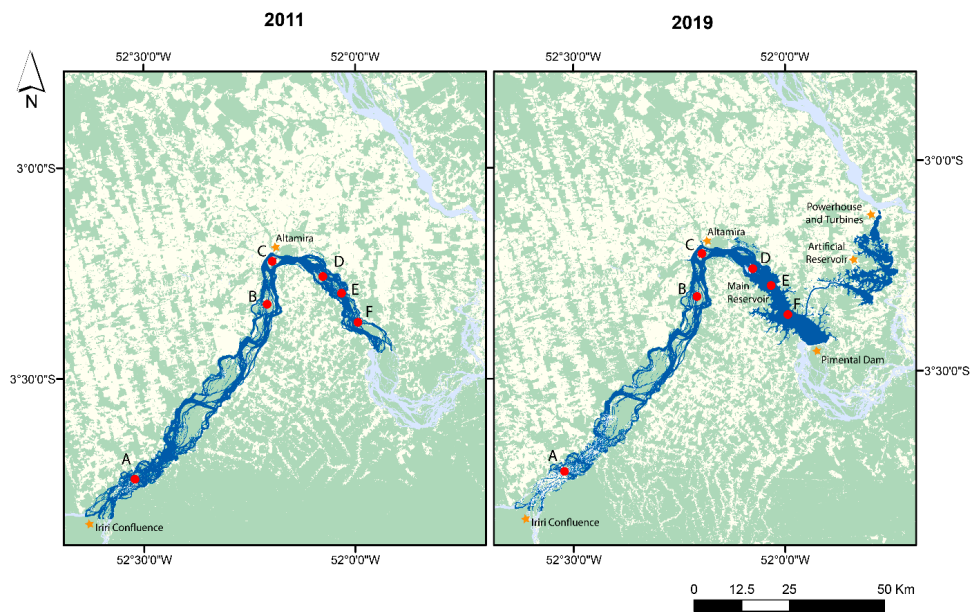


Figure 1. (A) Satellite imagery (NIR/Red/Green composite) from which the surface water classification datasets were generated (B) Surface water classification described here. Dark blue illustrates the surface water classification for the year 2011 from RapidEye and 2019 from PlanetScope imagery. The letters A–F locate points of comparison shown in Figure 2.

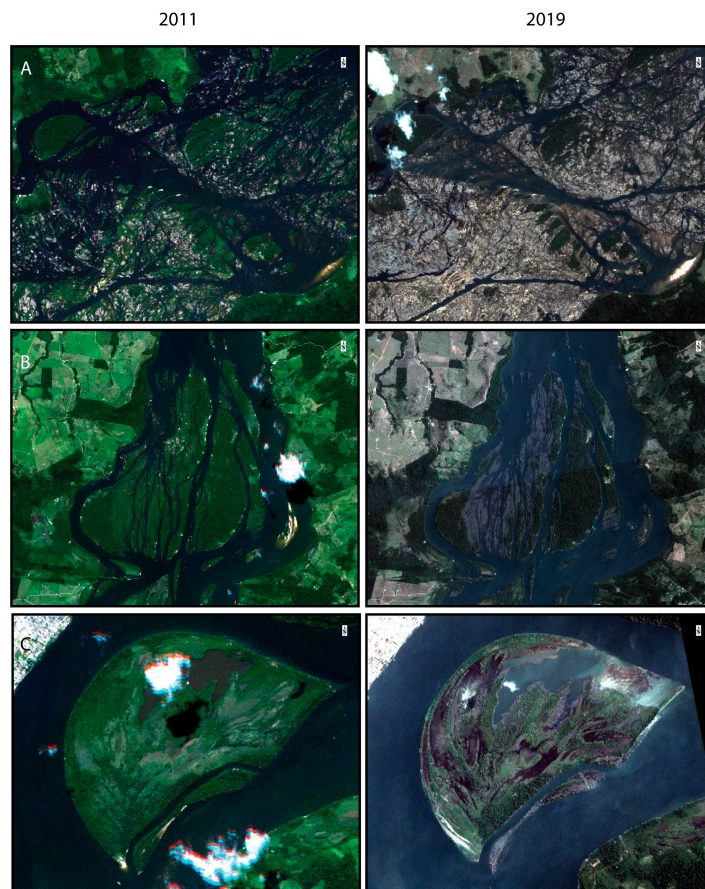


Figure 2. Cont.

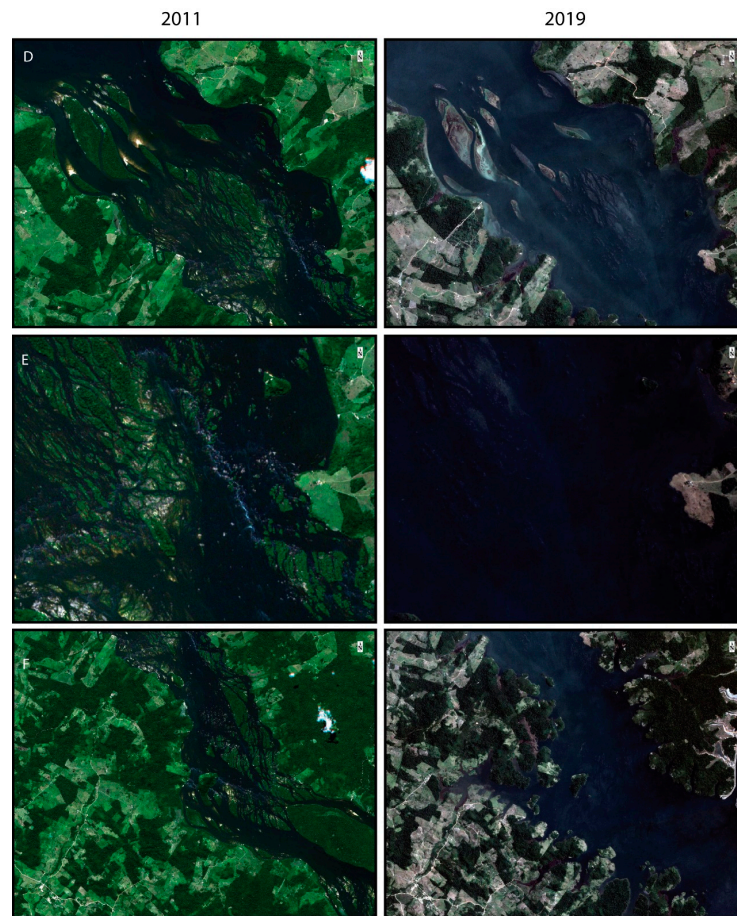


Figure 2. Points of comparison between the 2011 and 2019 satellite imagery. In (A), the difference in water level is attributed to yearly and seasonal differences in flow. The 2019 imagery was acquired later in the dry season (August) than the 2011 imagery (July). This area near the confluence with the Iriiri river is outside of the influence of the main reservoir. Both (B) and (C) are within the range of the impacts of the main reservoir. A higher water level and clearing of vegetation from the islands can be seen in 2019 in comparison to 2011 (B,C). These comparisons are downstream of Altamira in the sector of the river with the greatest change caused by the main reservoir of the Pimental dam. Many islands can be seen in 2011 (D–F) which are underwater in 2019. In F, the intake for the canal can be seen on the eastern side of the image from 2019.

3. Methods

The 2011 dataset is a classification of 10 RapidEye scenes acquired on 4 July (Figure 1A, Table 1). The RapidEye constellation is comprised of five satellites, each with a multispectral pushbroom imager acquiring five bands from the blue to the near infrared wavelengths. The images are acquired at a nadir ground sampling distance (GSD) of 6.5 m. The orthorectified imagery used here (level 3A) is produced at a 5 m pixel size [17].

The 2019 dataset is a classification of 23 PlanetScope scenes acquired between 24 July and 24 August (Table 2). PlanetScope is a constellation of more than 130 3U form factor CubeSats. The majority of the images used for the classification are from Dove PS satellites [18]. Their 2D frame detector has 6600 columns \times 4400 rows. The detector uses a Bayer pattern filter separating the blue, green and red channels. The top half (2200 rows) are used for the RGB bands; a NIR filter restricts the wavelengths of light. In the lower 2200 rows, another filter blocks all but the NIR wavelengths. The RGB half is combined in processing with the NIR half to produce four-band multispectral scenes [18]. Our classification also utilized one image from a next-generation Dove-R PS2.SD satellite (Table 2). The PS2.SD instrument utilizes the same detector as the PS, but rather than a Bayer filter and NIR band-pass filter, a butcher

block filter design segments the detector into four sections of 1100 rows of pixels, each with its own filter for one of the four spectral bands. The final multispectral scene is generated by stacking a number of consecutive frames on either side of a given frame [18]. All PlanetScope images used here are ‘multispectral analytic surface reflectance’ products (acquired at 3.7 m GSD, orthorectified to a 3 m pixel size) [19,20]. Figure 2 illustrates points of comparison between the imagery from the two years along the Iri to Pimental dam sector. Both the RapidEye and PlanetScope images were downloaded through a subscription from <https://www.planet.com/explorer>, the web interface to the catalogue of imagery from satellites managed by Planet Labs.

Table 1. RapidEye scenes used for the 2011 surface water classification.

Date (DD-MM-YY)	Scene ID	Satellite
04-07-11	2237610	RE2
04-07-11	2237609	RE2
04-07-11	2237509	RE2
04-07-11	2237510	RE2
04-07-11	2237508	RE2
04-07-11	2237410	RE2
04-07-11	2237408	RE2
04-07-11	2237409	RE2
04-07-11	2237307	RE2
04-07-11	2237308	RE2

Table 2. PlanetScope scenes used for the 2019 surface water classification.

Date (DD-MM-YY)	Scene ID	Satellite	Sector
24-07-19	132529	101f	Artificial reservoir
24-07-19	132530	101f	Artificial reservoir
24-07-19	132531	101f	Artificial reservoir
24-07-19	132532	101f	Artificial reservoir
11-08-19	130512	1020	Iri to Pimental
11-08-19	130514	1020	Iri to Pimental
11-08-19	130515	1020	Iri to Pimental
11-08-19	130516	1020	Iri to Pimental
11-08-19	130517	1020	Iri to Pimental
11-08-19	132859	1006	Iri to Pimental
11-08-19	132900	1006	Iri to Pimental
13-08-19	143914	53-106a ¹	Iri to Pimental
24-08-19	130314	104e	Iri to Pimental
24-08-19	130315	104e	Iri to Pimental
24-08-19	130316	104e	Iri to Pimental
24-08-19	130317	104e	Iri to Pimental
24-08-19	130318	104e	Iri to Pimental
24-08-19	130632	1020	Iri to Pimental
24-08-19	132930	0f17	Iri to Pimental
24-08-19	132931	0f17	Iri to Pimental
24-08-19	132932	0f17	Iri to Pimental
24-08-19	132933	0f17	Iri to Pimental
24-08-19	132934	0f17	Iri to Pimental
11-07-19	132719 ²	1032	Artificial reservoir

¹ This image is from a next generation Dove-R PS2.SD instrument, all others are from Dove PS instruments. ² This image was not used in the classification. It was only used as a guide in editing the vertices of the surface water polygons contaminated by cloud cover in the final classification.

The images from Tables 1 and 2 were classified through a GEOBIA approach in eCognition Developer 9.4 (Trimble Geospatial, Sunnyvale, CA, USA). The objective of GEOBIA is to improve upon and replicate human interpretation of imagery in an automated manner [21], allowing for large areas

to be analyzed efficiently [14], and is effective for land cover classifications of high spatial resolution imagery with a low spectral resolution [16,22]. Images were first segmented with the multiresolution segmentation algorithm using the following parameters: scale = 75, shape = 0.1 and compactness = 0.5. This algorithm is a bottom-up process that begins with one-pixel objects, and through an iterative process, merges neighboring pixels based on the relative homogeneity criteria of shape and colour [23]. Each of the four bands had different weights applied for the segmentation to maximize the separation of water from other materials: blue = 0.2, green = 0.2, red = 0.5 and NIR = 1 (Figure 3). For consistency, the red-edge band from RapidEye was not used. Training samples of segments representing “water”, “forest,” “non-forest” and “cloud” were manually selected. For classification, the nearest neighbor feature space was comprised of object level mean values of all four bands, brightness (average of the means of the four bands), maximum difference (maximum difference between bands) and the standard deviations of the objects in all four bands. These metrics served as the training data for a nearest neighbor classification.

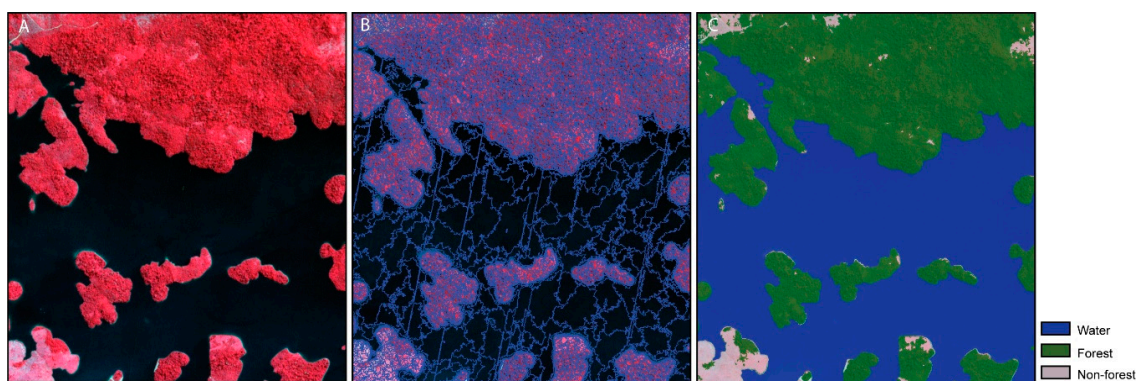


Figure 3. (A) Example of a NIR/Red/Green false color composite of a part of PS scene 132,531 (2019) from the artificial reservoir. (B) Outlines of the segments from the same image as shown in (A). (C) Final GEOBIA classification of the segments into water, forest, and non-forest classes.

The individual classifications were simplified to “water” and “land” classes through a decision tree in ENVI 5.5 (L3 Harris Geospatial, Boulder, CO, USA) and mosaicked into a single binary raster for each period (2011 and 2019). The mosaics were converted to polygon datasets in ArcMap 10.7 (ESRI, Redlands, CA). Polygons representing the “land” class were removed and each water polygon was inspected through an overlay with the image from which it was generated. Erroneous water polygons, such as those representing dark shadows (from topography or tree crowns), were removed. For the few areas where small clouds obstructed the shoreline, the polygon vertices were edited to trace the shoreline without cloud contamination (Figure 4). Baseline images from either WorldView 1 (acquired in 2011) or other PlanetScope scenes acquired close to the date of the classification (Table 2) were used to guide the vertex editing.

The final edited polygon layer was dissolved to create a single polygon layer representing surface water. For validation, mosaics of the imagery (Tables 1 and 2) were created and points representing water and land were generated through visual interpretation of the image mosaics. Tables 3 and 4 illustrate the confusion matrices for the two classifications. For 2011, 658 and 885 points were generated for water and land (consisting of rock, sand, or vegetation), respectively. For 2019, 750 and 813 points were generated for water and land, respectively. The points were generated throughout the entire study area. Boundary (edge) pixels between classes were avoided due to the potential mixing of materials in these pixels.

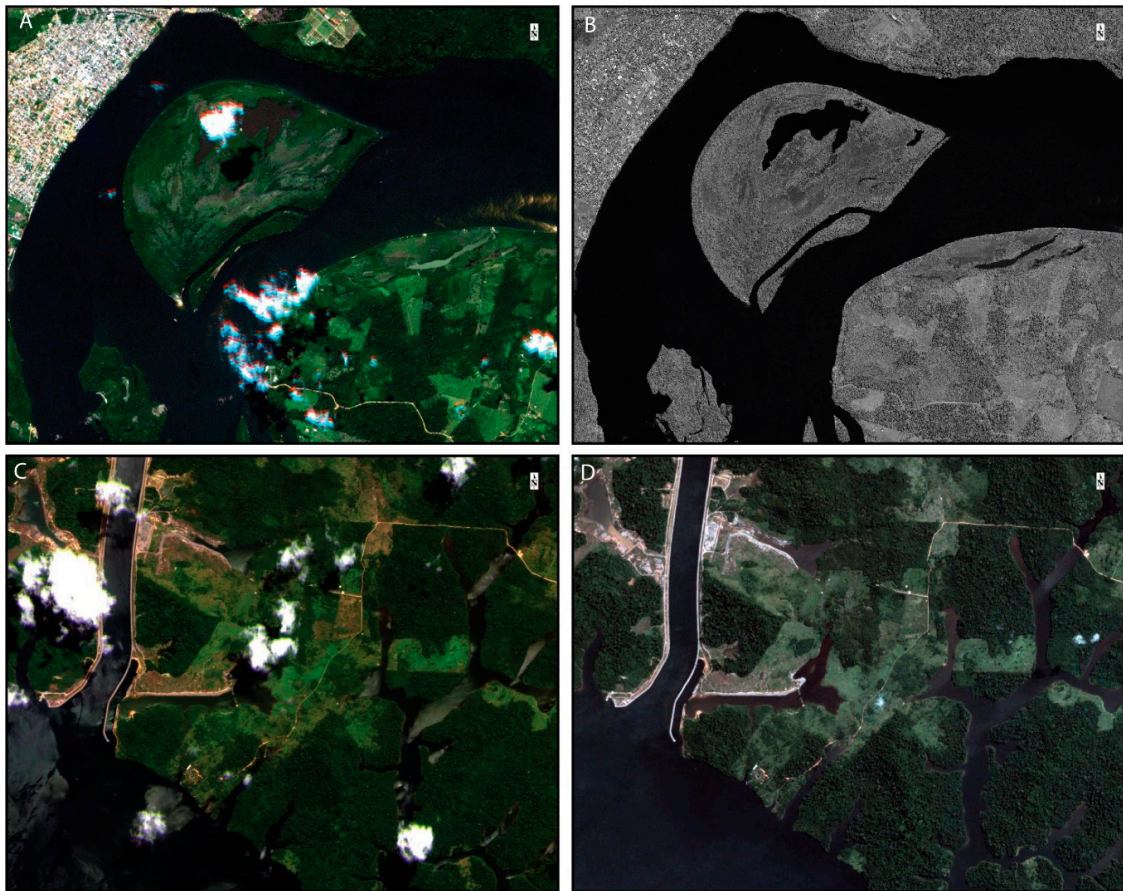


Figure 4. (A) RapidEye imagery from Arapujá island (4 July 2011) with cloud contamination obscuring the shoreline. (B) Worldview 1 imagery over the same area as A, acquired on 17 June 2011, used as a baseline to edit the shoreline vertices from the RapidEye classification in areas of cloud contamination. (C) PlanetScope imagery from 13 August 2019 of the entrance to the artificial reservoir with cloud contamination and sun glint artifacts. (D) PlanetScope imagery from the same area as (C), acquired on 11 July 2019, used as a baseline to edit the shoreline vertices from the PlanetScope classification in areas of cloud contamination.

Table 3. Confusion matrix for the 2011 classification.

	Water-Reference	Land-Reference	User's Accuracy (%)
Water-Classification	654	45	93.6
Land-Classification	4	840	99.5
Producer's Accuracy (%)	99.4	94.9	OA = 96.8

Table 4. Confusion matrix for the 2019 classification.

	Water-Reference	Land-Reference	User's Accuracy (%)
Water-Classification	748	1	99.9
Land-Classification	2	812	99.8
Producer's Accuracy (%)	99.7	99.9	OA = 99.8

The total surface water area was calculated as 426.89 km² for 2011 and 569.63 km² for 2019. We estimate the surface area within the impact zone of the main reservoir to be 220.9 km² in 2011 and 426.4 km², a difference of 205.5 km². Figure 5 illustrates the area of greatest change in surface water extent from the Xingu's confluence with the Iriri river to the Pimental dam (including the artificial reservoir) following the operationalization of the Belo Monte dam.

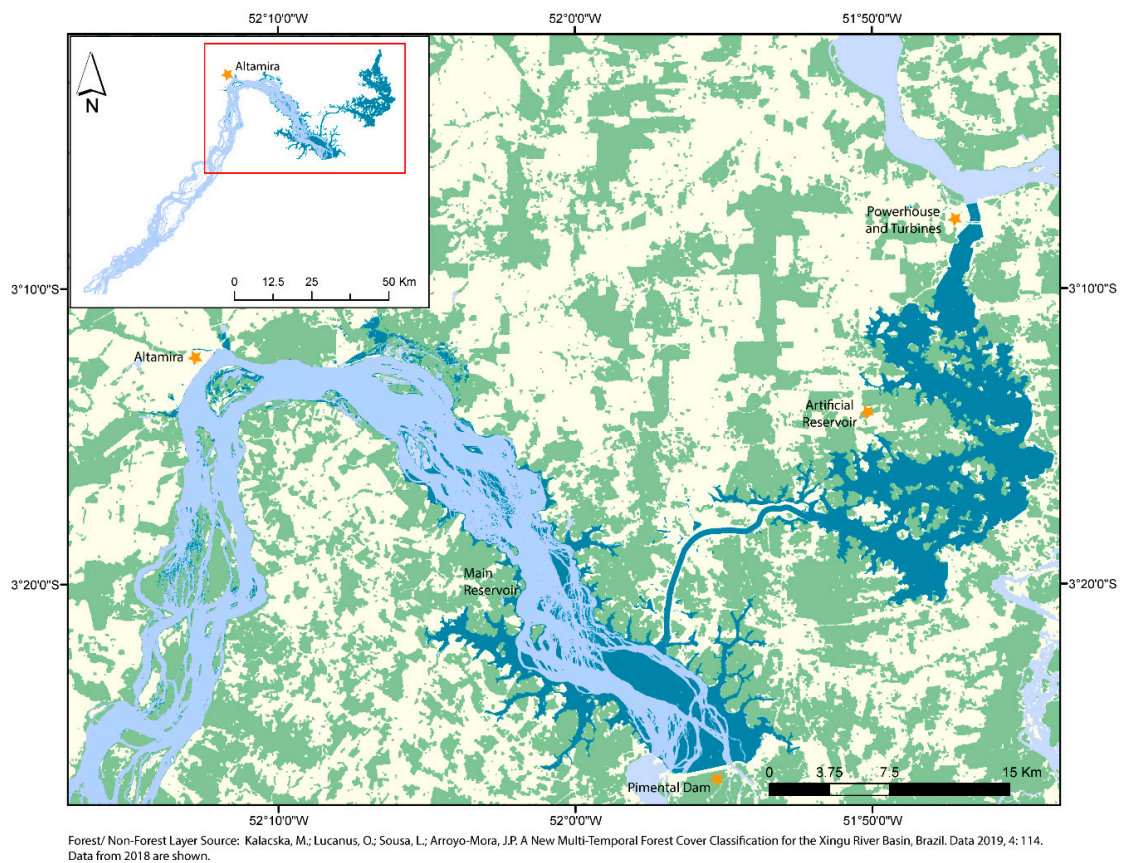


Figure 5. Map illustrating the area of greatest change in surface water extent pre and post operationalization of the Belo Monte dam. The light blue illustrates the classification from 2011, while the dark blue illustrates the classification from 2019.

4. User Notes

The fine spatial resolution of the imagery from both RapidEye and PlanetScope allowed for an accurate and more detailed classification of surface water than is possible from moderate resolution optical satellite imagery such as Landsat (30 m) or Sentinel-2 (10–60 m) (e.g., [12]). There are many different types of rocks, soils and landforms that comprise the shoreline and small islands (Figures 6 and 7). In areas of higher flow, riverweed (*Podostomaceaea*) can be found adhering to rocks in a range of states from dry plants to green leaves and flowers (Figure 6). These all add to the complexity of the classification. Despite the benefits the 3–5 m pixel sizes provide, some challenges remain where some features are smaller than a pixel. Channels that are narrower than the pixel size of the imagery are likely to have been missed in the classification. Small boulders (e.g., Figure 7) in the river may have been misclassified as water if they occupied less than a pixel in area. Conversely, large patches of dead trees in forest flooded by the reservoir (e.g., Figure 7) that occupy areas larger than a pixel may have led to false negatives in the classification.



Figure 6. Field photos showing a range of rock types and sand that are present in the study area outside of the impact zone of the dam located within the pre-Cambrian Complex of the Xingu (see [24] for a description of the geology of the region). Dry and live riverweed (*Podostomaceae*) can be seen covering many of the surfaces ranging in colour from green and brown (leaves) to pink (flowers) and white (dry plants). Many of the rock formations are smaller than medium spatial resolution satellite imagery (e.g., 30 m Landsat or 10 m Sentinel-2).

Furthermore, it is important to take into consideration the highly seasonal water flow and the natural flood pulse of the river. The river has four hydrological periods, low water (September–November), flooding (December–February), high water (March–May) and receding water (June–August) [25], with discharge rates ranging from, on average, ~ 2000 m³/s in October to $\sim 21,000$ m³/s in April [8]. It has one of the highest annual variations in flow of all Amazon tributaries. The imagery from 2011 (4 July) is earlier in the receding period than that of 2019 (11–24 August) due to the availability of imagery with minimal cloud cover for the entire area. There is an approximate 1000 m³/s difference in discharge between July and August [8]. The effect of this difference can be seen in the southern sector of the data near the confluence of the Iriri river, outside the impact zone of the reservoir. In Figure 2A, for example, the higher water level is seen in the RapidEye imagery from 2011 in comparison to the PlanetScope image from 2019, where there is a larger amount of rock exposed in

the channels. With continuous acquisition of daily revisit satellite imagery, over time it may be possible to acquire minimal cloud cover imagery for the high water periods as well, providing a more thorough assessment of the seasonal extents of the river.



Figure 7. Field photos from the zone impacted by the reservoir at the boundary of the pre-Cambrian Complex of the Xingu and the Amazon Sedimentary Basin (see [24] for a description of the geology of the region). The rock formations differ in this sector compared to Figure 6. Cleared islands with flooding and flooded forest (vegetation not cleared prior to flooding) from within the reservoir near the Pimental dam can also be seen.

Author Contributions: Conceptualization, M.K.; formal analysis, M.K., O.L.; investigation, M.K., O.L., L.S.; writing—original draft preparation, M.K., O.L., L.S.; writing—review and editing, M.K., O.L., L.S., J.P.A.-M.; visualization, J.P.A.-M; All authors have read and agreed to the published version of the manuscript.

Funding: This research was funded by a Discovery Grant from the Natural Sciences and Engineering Research Council of Canada to Kalacska. Sousa was supported by a productivity grant from CNPq (#309815/2017-7) and a CNPq Universal Project grant #486376/2013-3. Access to PlanetScope and RapidEye imagery was provided by the Department of Geography, McGill University. Worldview 1 imagery was provided by an imagery grant from the Digital Globe Foundation to Kalacska.

Conflicts of Interest: The authors declare no conflict of interest. The funders had no role in the design of the study; in the collection, analyses, or interpretation of data; in the writing of the manuscript, or in the decision to publish the results.

References

1. Dagosta, F.C.P.; De Pinna, M. The fishes of the Amazon: Distribution and biogeographical patterns, with a comprehensive list of species. *Bull. Am. Mus. Nat. Hist.* **2019**, *431*, 1–163. [[CrossRef](#)]
2. Camargo, M.; Giarrizzo, T.; Isaac, V. Review of the geographic distribution of fish fauna of the Xingu river basin. *Ecotropica* **2004**, *10*, 123–147.
3. Jézéquel, C.; Tedesco, P.A.; Bigorne, R.; Maldonado-Ocampo, J.A.; Ortega, H.; Hidalgo, M.; Martens, K.; Torrente-Vilara, G.; Zuanon, J.; Acosta, A.; et al. A database of freshwater fish species of the Amazon Basin. *Sci. Data* **2020**, *7*, 96. [[CrossRef](#)] [[PubMed](#)]
4. Bratman, E.; Dias, C.B. Development blind spots and environmental impact assessment: Tensions between policy, law and practice in Brazil's Xingu river basin. *Environ. Impact Assess. Rev.* **2018**, *70*, 1–10. [[CrossRef](#)]
5. Perez, M.S. Where the Xingu bends and will soon break. *Am. Sci.* **2015**, *103*, 395–397. [[CrossRef](#)]
6. Latrubesse, E.M.; Arima, E.Y.; Dunne, T.; Park, E.; Baker, V.R.; d'Horta, F.M.; Wight, C.; Wittmann, F.; Zuanon, J.; Baker, P.A.; et al. Damming the rivers of the Amazon basin. *Nature* **2017**, *546*, 363–369. [[CrossRef](#)] [[PubMed](#)]
7. Winemiller, K.O.; McIntyre, P.B.; Castello, L.; Fluet-Chouinard, E.; Giarrizzo, T.; Nam, S.; Baird, I.G.; Darwall, W.; Lujan, N.K.; Harrison, I.; et al. Balancing hydropower and biodiversity in the Amazon, Congo, and Mekong. *Science* **2016**, *351*, 128–129. [[CrossRef](#)] [[PubMed](#)]
8. de Araújo, K.R.; Sawakuchi, H.O.; Bertassoli Jr, D.J.; Sawakuchi, A.O.; da Silva, K.D.; Vieira, T.B.; Ward, N.D.; Pereira, T.S. Carbon dioxide (CO₂) concentrations and emission in the newly constructed Belo Monte hydropower complex in the Xingu River, Amazonia. *Biogeosciences* **2019**, *16*, 3527–3542. [[CrossRef](#)]
9. Fearnside, P.M. Dams in the Amazon: Belo Monte and Brazil's hydroelectric development of the Xingu River basin. *Environ. Manag.* **2006**, *38*, 16. [[CrossRef](#)] [[PubMed](#)]
10. Fearnside, P.M. Greenhouse gases in the environmental impact study for the Belo Monte Hydroelectric Dam. *Novos Cad. NAEA* **2011**, *14*, 5–19.
11. Fearnside, P.M. Belo Monte: Actors and arguments in the struggle over Brazil's most controversial Amazonian dam. *DIE ERDE J. Geogr. Soc. Berl.* **2017**, *148*, 14–26. [[CrossRef](#)]
12. Pekel, J.F.; Cottam, A.; Gorelick, N.; Belward, A.S. High-resolution mapping of global surface water and its long-term changes. *Nature* **2016**, *540*, 418–422. [[CrossRef](#)] [[PubMed](#)]
13. MapBiomas Project. MapBiomas Project-Collection v3.1 of the Annual Land Use Land Cover Maps of Brazil. Available online: <https://mapbiomas.org/en> (accessed on 1 August 2019).
14. Demarchi, L.; van de Bund, W.; Pistocchi, A. Object-based ensemble learning for pan-european riverscape units mapping based on copernicus VHR and EU-DEM data fusion. *Remote Sens.* **2020**, *12*, 1222. [[CrossRef](#)]
15. Kalacska, M.; Arroyo-Mora, J.P.; Lucanus, O.; Sousa, L.; Pereira, T.; Vieira, T. Deciphering the many maps of the Xingu—an assessment of land cover classifications at multiple scales. *bioRxiv* **2019**. [[CrossRef](#)]
16. Chen, G.; Weng, Q.H.; Hay, G.J.; He, Y.N. Geographic object-based image analysis (GEOBIA): Emerging trends and future opportunities. *Gisci. Remote Sens.* **2018**, *55*, 159–182. [[CrossRef](#)]
17. RapidEye, A.G. Satellite Imagery Product Specifications. Available online: <https://www.planet.com/products/satellite-imagery/files/160625-RapidEye%20Image-Product-Specifications.pdf> (accessed on 5 June 2020).
18. Planet Team. Understanding PlanetScope Instruments. Available online: <https://developers.planet.com/docs/data/sensors/> (accessed on 5 June 2020).
19. Planet Team. *Planet Imagery Product Specification: PlanetScope & RapidEye*; Planet: San Francisco, CA, USA, 2016. Available online: https://www.planet.com/products/satellite-imagery/files/1610.06_Spec%20Sheet_Combined_Imagery_Product_Letter_ENGv1.pdf (accessed on 5 June 2020).
20. Planet Team. *Planet. Surface Reflectance v2.0*; Planet: San Francisco, CA, USA. p. 18. Available online: https://assets.planet.com/marketing/PDF/Planet_Surface_Reflectance_Technical_White_Paper.pdf (accessed on 5 June 2020).

21. Johansen, K.; Sohlbach, M.; Sullivan, B.; Stringer, S.; Peasley, D.; Phinn, S. Mapping banana plants from high spatial resolution orthophotos to facilitate plant health assessment. *Remote Sens.* **2014**, *6*, 8261–8286. [[CrossRef](#)]
22. Ma, L.; Li, M.C.; Ma, X.X.; Cheng, L.; Du, P.J.; Liu, Y.X. A review of supervised object-based land-cover image classification. *ISPRS J. Photogramm. Remote Sens.* **2017**, *130*, 277–293. [[CrossRef](#)]
23. Benz, U.C.; Hofmann, P.; Willhauck, G.; Lingenfelder, I.; Heynen, M. Multi-resolution, object-oriented fuzzy analysis of remote sensing data for GIS-ready information. *ISPRS J. Photogramm. Remote Sens.* **2004**, *58*, 239–258. [[CrossRef](#)]
24. Silva, J.P.; Pereira, D.I.; Aguiar, A.M.; Rodrigues, C. Geodiversity assessment of the Xingu drainage basin. *J. Maps* **2013**, *9*, 254–262. [[CrossRef](#)]
25. Barbosa, T.A.P.; Rosa, D.C.O.; Soares, B.E.; Costa, C.H.A.; Esposito, M.C.; Montag, L.F.A. Effect of flood pulses on the trophic ecology of four piscivorous fishes from the eastern Amazon. *J. Fish Biol.* **2018**, *93*, 30–39. [[CrossRef](#)] [[PubMed](#)]



© 2020 by the authors. Licensee MDPI, Basel, Switzerland. This article is an open access article distributed under the terms and conditions of the Creative Commons Attribution (CC BY) license (<http://creativecommons.org/licenses/by/4.0/>).